Reactor neutrino liquid xenon coherent elastic scattering experiment

Chang Cai,¹ Guocai Chen,² Jiangyu Chen,³ Rundong Fang,⁴ Fei Gao,¹,∗ Xiaoran Guo,⁵,⁶ Jiheng Guo,⁴ Tingyi He,⁻,† Chengjie Jia,¹,‡ Gaojun Jin,² Yipin Jing,¹,§ Gaojun Ju,² Yang Lei,¹ Jiayi Li,¹ Kaihang Li,¹ Meng Li,² Minhua Li,² Shengchao Li,ጾ Siyin Li,ጾ Tao Li,² Qing Lin,⁵,⁶ Jiajun Liu,⁰ Minghao Liu,¹ Sheng Lv,² Guang Luo,⁰ Jian Ma,¹ Chuanping Shen,² Mingzhuo Song,¹ Lijun Tong,⁵,⁶ Xiaoyu Wang,ጾ Wei Wang,³,⁰ Xiaoping Wang,⁴,¹0 Zihu Wang,² Yuehuan Wei,³,¶ Liming Weng,² Xiang Xiao,⁰ Lingfeng Xie,¹ Dacheng Xu,¹,∥ Jijun Yang,ጾ Litao Yang,¹¹ Long Yang,² Jingqiang Ye,⁻ Jiachen Yu,⁵,⁶ Qian Yue,¹¹¹ Yuyong Yue,³ Bingwei Zhang,² Shuhao Zhang,¹ Yifei Zhao,¹ and Chenhui Zhu⁶ (RELICS Collaboration)

¹Department of Physics & Center for High Energy Physics, Tsinghua University, Beijing 100084, China

²CNNC Sanmen Nuclear Power Company, Zhejiang 317112, China

³Sino-French Institute of Nuclear Engineering and Technology, Sun Yat-Sen University, Zhuhai 519082, China

⁴School of Physics, Beihang University, Beijing 100083, China

⁵State Key Laboratory of Particle Detection and Electronics,

University of Science and Technology of China, Hefei 230026, China

⁶Department of Modern Physics, University of Science and Technology of China, Hefei 230026, China

⁷School of Science and Engineering, The Chinese University of

Hong Kong (Shenzhen), Shenzhen, Guangdong, 518172, P.R. China

⁸School of Science, Westlake University, Hangzhou 310030, China

⁹School of Physics, Sun Yat-Sen University, Guangzhou 510275, China

¹⁰Beijing Key Laboratory of Advanced Nuclear Materials and Physics, Beihang University, Beijing 100191, China

¹¹Key Laboratory of Particle and Radiation Imaging (Ministry of Education) & Department of Engineering Physics, Tsinghua University, Beijing 100084, China

(Dated: October 22, 2024)

Coherent elastic neutrino-nucleus scattering ($CE\nu NS$) provides a unique probe for neutrino properties Beyond the Standard Model (BSM) physics. REactor neutrino LIquid xenon Coherent Scattering experiment (RELICS), a proposed reactor neutrino program using liquid xenon time projection chamber (LXeTPC) technology, aims to investigate the $CE\nu NS$ process of antineutrinos off xenon atomic nuclei. In this work, the design of the experiment is studied and optimized based on Monte Carlo (MC) simulations. To achieve a sufficiently low energy threshold for $CE\nu NS$ detection, an ionization-only analysis channel is adopted for RELICS. A high emission rate of delayed electrons after a big ionization signal is the major background, leading to an analysis threshold of 120 photo-electrons in the $\text{CE}\nu\text{NS}$ search. The second largest background, nuclear recoils induced by cosmic-ray neutrons, is suppressed via a passive water shield. The physics potential of RELICS is explored with a 32 kg·yr exposure at a baseline of 25 m from a reactor core with a 3 GW thermal power. In an energy range of 120 to 300 PE, corresponding to an average nuclear recoil from 0.63 to 1.36 keV considering the liquid xenon response and detector-related effect, we expect 4639.7 CE ν NS and 1687.8 background events. The sensitivity of RELICS to the weak mixing angle is investigated at a low momentum transfer. Our study shows that RELICS can further improve the constraints on the non-standard neutrino interaction (NSI) compared to the current best results.

PACS numbers:

Keywords:

Keywords: $CE\nu NS$, reactor neutrino, liquid xenon, LXeTPC, MC

* Corresponding author: feigao@tsinghua.edu.cn

I. INTRODUCTION

Coherent elastic neutrino-nucleus scattering (CE ν NS) is a Standard Model (SM) weak neutral current process postulated in 1974 [1]. The incoming neutrino sees the nucleus as a whole during scattering with a cross-section proportional to the nucleon number squared in the full coherency regime when the neutrino energy is smaller than $\sim \! \! 10 \, \text{MeV}.$ Despite this process having a relatively large cross-section, the detection is challenging due to the ultra-low deposited energy in keV or sub-keV nuclear recoil scale. This process had evaded experimental discov-

 $^{^\}dagger$ Also at College of Physics, Chongqing University, Chongqing 401331, China

[‡] Now at Department of Physics, Stanford University, Stanford, CA 94305, USA

[§] Also at School of Physics, Jilin University, Jilin 130012, China

[¶] Corresponding author: weiyh29@mail.sysu.edu.cn

Now at Physics Department, Columbia University, New York, NY 10027, USA.

eries for decades until 2017 when it was first observed by the COHERENT collaboration with neutrinos produced by the Spallation Neutron Source (SNS) at Oak Ridge National Laboratory scattering off a CsI scintillator [2], and later confirmed with a liquid argon detector [3] in 2020. These measurements of $CE\nu NS$ offer new probes for diverse physical phenomena.

 $\text{CE}\nu\text{NS}$ can provide new constraints on the SM physics and the physics Beyond it (BSM). The weak mixing angle is related to the $CE\nu NS$ cross-section [4]. Any deviation from the SM prediction in measurement can be an indication of new physics. $CE\nu NS$ is also a valuable tool to constrain nonstandard neutrino interactions (NSI) [5], to search for sterile neutrinos [6], to verify the existence of non-trivial neutrino electromagnetic properties [7], to study the nuclear structure [8] and understand the core-collapse supernova explosions [9]. In addition, the $CE\nu NS$ signal from the solar or atmospheric neutrinos is expected to be an irreducible background for the next-generation dark matter direct detection experiments, such as PandaX-xT [10] and XLZD [11] using xenon as detection target [12, 13]. A precise measurement of this process, especially one with a xenon target, can provide valuable information for dark matter experiments digging into the so-called "neutrino floor/fog" [14– 16].

The observation of $CE\nu NS$ by the COHERENT collaboration opened the way to $CE\nu NS$ experimental studies. While the neutrino beam has been the primary source for the $CE\nu NS$ discovery, the anti-neutrino from nuclear reactors provides an alternative chance for $\text{CE}\nu \text{NS}$ detection. Therefore, the nuclear reactors with large antineutrino fluxes delivered with typical energies of a few MeV, which is in the full coherency regime of $CE\nu NS$, have been proposed as attractive complementary facilities for several $\text{CE}\nu\text{NS}$ experiments. Due to the considerably low recoil energy and complex background, the reactor $CE\nu NS$ is harder to detect. Many efforts are underway with reactor neutrinos, such as [17–28]. Benefiting from the higher flux and lower energy of reactor neutrinos compared with the SNS neutrino beam, the detection of reactor $CE\nu NS$ can provide a complementary sensitivity in most fields of the physical phenomena mentioned above through new couplings [29, 30], and also potential applications such as nuclear safeguards [31].

In this context, RELICS is a reactor neutrino experiment using liquid xenon time projection chamber (LXeTPC) technology. LXeTPC is one of the leading technologies for rare event searches, such as detecting dark matter and neutrinoless double beta decay [11, 32–36]. Benefiting from its ultra-low threshold by using ionization-only channel [37, 38] and reduced background, the LXeTPC is an excellent approach for reactor CE ν NS detection. The RELICS experiment is proposed to be located near the Sanmen Nuclear Power Plant in Zhejiang province, China. At a \sim 25 m baseline to the \sim 3 GW reactor core, the average neutrino flux available for RELICS is \sim 10¹³cm⁻²s⁻¹.

This work is organized as follows. The operation principle and the design of the detector as well as the shielding system, are described in detail in section II. The simulation framework is introduced in section III. In section IV, we predict the expected $\text{CE}\nu\text{NS}$ event rates from the Sanmen nuclear reactor. Section V discusses a dedicated simulation of background contributions. The physics potential of RELICS is provided in section VI. A summary is presented in section VII.

II. EXPERIMENTAL DESIGNS

A. RELICS detector

The LXeTPC technology consists in measuring the energy deposited from particle interactions by simultaneously detecting the prompt scintillation light (S1) and delayed ionization charge (S2) [39]. The S1 is produced by the direct excitation of xenon atoms and the recombination of electron-ion pairs in LXe. The S2 is proportional to the number of liberated electrons extracted into gas xenon (GXe), which are then amplified via electroluminescence. Both S1 and S2 are recorded by photosensors, usually photomultiplier tubes (PMTs), on top and bottom arrays of the TPC. This allows a three-dimensional (3D) vertex reconstruction with a sub-centimeter precision, and the S2/S1 ratio can be used to discriminate between nuclear recoil (NR) and electronic recoil (ER) for background reduction. Typically, the energy threshold of LXeTPC is limited by the S1 signal in the range of \sim (2-3) photo-electrons (PEs). The inherent S2 amplification provides an alternative approach to decrease the energy threshold by utilizing the ionization-only channel, usually called the "S2-only" analysis. This approach can reduce the energy threshold to a few ionization electrons (equivalent NR energy below $1\,\mathrm{keV_{nr}})$ by sacrificing the NR/ER discrimination and depth information, which, in the case of $CE\nu NS$ detection, can be largely compensated by the high signal-to-background ratio profited from the intense reactor neutrino flux.

A preliminary 3D mechanical design of the RELICS detector is shown in figure 1. A cylindrical TPC of 24 cm in height and 28 cm in diameter sits in a double-layer stainless steel (S.S) vessel, which provides a stable cryogenic environment. The target volume containing an active LXe of approximately 44 kg is defined by 12 interlocking and light-tight PTFE (polytetrafluoroethylene, Teflon) panels. The active LXe is then viewed by two arrays of 64 Hamamatsu R8520-406 PMTs on top and bottom. A fiducial mass of 32 kg LXe with only a radius selection of 12 cm can be well-defined for $\text{CE}\nu\text{NS}$ search under "S2-only" analysis. A "diving bell" structure is mounted above the top PMT array to control the liquid level. Five etched S.S electrodes, including two grounding screenings on top and bottom to protect PMTs from high voltage (HV), anode, gate, and cathode to provide a nominal drift field of 500 V/cm and an extraction field of

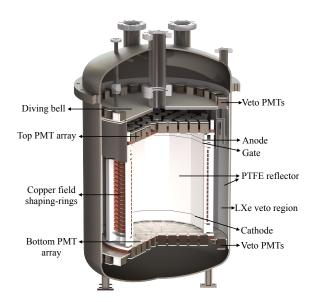


FIG. 1. The RELICS detector with the inner S.S. vessel, diving bell, veto PMTs, and the center TPC consisting of the top and bottom PMT arrays, anode, gate and cathode electrodes, copper field shaping-rings and PTFE reflector.

 $10\,\mathrm{kV/cm}$ in GXe, are installed. To ensure the uniformity of the drift field, the target volume is encircled by several field-shaping rings made from oxygen-free high thermal conductivity (OFHC) copper. The TPC is surrounded by approximately 62 kg of LXe, which acts as a 4π active veto for background suppression. The LXe veto volume is instrumented with 48 R8520-406 PMTs. To achieve a high light collection, the inner surface of the inner vessel is covered with a thin PTFE foil. It is worth noting that the LXe veto is designed to reduce the background by ~ 5 times by removing the coincidence events inside TPC and in the LXe veto layer. All materials for the detector construction will be carefully selected to ensure low intrinsic radioactivity.

B. Shielding system

Near-reactor neutrino experiments usually operate with shallow overburdens. Thus, the high-energy cosmic-ray neutrons are supposed to be one of the main backgrounds for the NR searches from $\text{CE}\nu\text{NS}$. A sufficient neutron shielding structure, such as water, is required to slow down and absorb the neutrons. Meanwhile, the cosmic muon and its induced secondaries are expected to be another major background. A highly efficient active muon veto anti-coincidence system is also critical to the success of this type of experiment.

Figure 2 shows the design of the RELICS shielding system based on Monte Carlo (MC) simulations, which is detailed in section V. The design has been optimized to satisfy the requirement of the CE ν NS detection. The LXe detector is placed inside a shield of $7\,\mathrm{m}\times7\,\mathrm{m}\times7\,\mathrm{m}$ of wa-



FIG. 2. The LXe detector with a 8 cm thick PS muon veto detector inside a $7 \,\mathrm{m} \times 7 \,\mathrm{m} \times 7 \,\mathrm{m}$ S.S water shield tank. The center of the LXe detector is $2 \,\mathrm{m}$ above ground.

ter contained in a S.S tank. A 5 m water shield on top can suppress the cosmic-ray neutron-induced background to a controlled level. With such a water tank, the external neutrons and gammas from the laboratory environment and the nuclear reactor can be reduced to negligible levels. In close to the LXe detector, a muon veto detector is installed. The veto detector is made of 8 cm thick plastic scintillator (PS) equipped with wavelength-shifting fibers and silicon photomultipliers (SiPMs) to collect and detect the scintillation light. A high veto efficiency of 99% is expected for the RELICS experiment.

III. SIMULATION FRAMEWORK

The MC simulation framework of the RELICS experiment (RelicsSim) is built upon a Geant4-based BambooMC toolkit [40]. Full detector geometry is implemented, including the detailed detector components and the shielding system. Various types of particle interactions are studied by simulation to evaluate the expected signal and background. Subsequently, RelicsAPT, which inherits from the Appletree [41] framework developed by XENONnT collaboration [42], is adopted to convert the energy depositions into observable S1 and S2 signals. The conversion is based on the intrinsic light yield (L_y) and charge yield (Q_y) in LXe, and convoluted with the detector-related signal detection and reconstruction ef-

fects.

A. Liquid xenon response

Particle interaction in LXe will produce photons and electrons. The NEST model can characterize this process [43] after considering the fluctuations in scintillation, ionization, electron-ion recombination, and their drift field dependence. In RelicsAPT, the L_u and Q_u from NEST (v2.3.6) at $500 \,\mathrm{V/cm}$ drift field are used with no uncertainty assigned for NRs larger than $3 \,\mathrm{keV_{nr}}$. To quantify the uncertainty of light and charge yields for $\text{CE}\nu \text{NS}$ events, the L_y and Q_y bands in XENON1T solar ⁸B neutrino search [44] are adopted for NRs less than $3 \,\mathrm{keV_{nr}}$. L_y and Q_y bands are scaled to make the center curve connected to NEST at $3 \,\mathrm{keV_{nr}}$. The final L_y and Q_v of NRs applied in RelicsAPT are shown in figure 3. These light and charge yield responses and their uncertainties comparable to the XENON1T model are chosen as a benchmark model in this analysis to illustrate its impact on the sensitivity to $CE\nu NS$ and new physics beyond the Standard Model. For ERs, L_y and Q_y from NEST (v2.3.6) are used without uncertainties. In the 4π LXe veto region, both L_y and Q_y are modeled with zero electric fields.

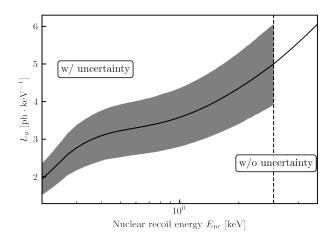
B. Detector related effects

In addition to the intrinsic LXe response model, the detector-related effects must be considered when interpreting the observed S1 and S2 signals. The main detector parameters are considered based on the expected detector performance listed in Tab. I, as a conservative estimation.

To explore the capability of the RELICS detector on the ionization-only detection channel, the light collection efficiency (LCE) of S2 is simulated by RelicsSim with the optical parameters listed in Tab. I. The LCE map is shown in figure 4. An averaged g_2 value of $30\,\mathrm{PE/e^-}$ is estimated based on the S2 LCE map, the properties of the PMTs, such as ϵ_{QE} , ϵ_{CE} , and p_{DPE} that also listed in Tab. I, and a 100% electron extraction efficiency on the liquid surface. An electron lifetime of 1.2 ms is applied for S2 estimation considering the probability of electrons loss to electronegative impurities during their drift. Under these hypotheses, we assume a 100% trigger efficiency at $4\,\mathrm{e^-}$ ($120\,\mathrm{PE}$) targeted detection threshold for RELICS sensitivity study.

IV. EXPECTED $CE\nu NS$ EVENTS

The SM of particle physics well predicts the $\text{CE}\nu\text{NS}$ process — a neutrino of any flavor scatters off a nucleus via Z^0 boson exchange coherently over the whole nucleus



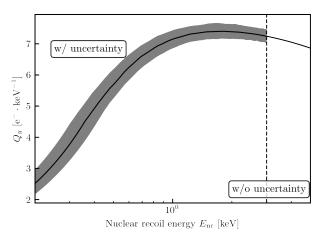


FIG. 3. The L_y (upper panel) and Q_y (lower panel) model of NR in RelicsAPT. For E_{nr} less than $3\,\mathrm{keV_{nr}}$, the XENON1T yields model in $^8\mathrm{B}$ neutrino search [44] is adopted, and scaled to NEST model at $3\,\mathrm{keV_{nr}}$. For E_{nr} larger than $3\,\mathrm{keV_{nr}}$, NEST model is used with 500 V/cm drift field.

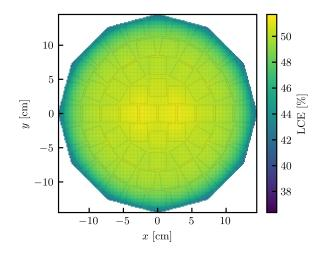


FIG. 4. The S2 LCE map with both top and bottom PMT arrays. Simulations are performed by generating S2 photons in the GXe region below the anode.

TABLE I. The detector related parameters.

Optical parameters				
PTFE reflectivity (LXe & GXe)	99% [45]			
LXe Rayleigh scattering length	$30{ m cm}[46]$			
LXe absorption length	$50\mathrm{m}[47]$			
Electrodes reflectivity	57% [48]			
Signal generation				
PMT quantum efficiency ($\epsilon_{\rm QE}$)	33% [49]			
PMT collection efficiency ($\epsilon_{\rm CE}$)	75% [49]			
Double PE probability (p_{DPE})	21.9% [50, 51]			
g_2	$30\mathrm{PE/e^-}$			
Detector operation				
Drift field	$500\mathrm{V/cm}$			
Electron lifetime	$1.2{ m ms}[32]$			

at a low momentum transfer $(Q = \sqrt{2m_t E_R})$. The differential cross-section can be written as Eq. 1 below:

$$\frac{d\sigma}{dE_R} = \frac{G_F^2}{2\pi} \frac{Q_w^2}{4} F^2 \left(2m_t E_R\right) m_t \left[2 - \frac{m_t E_R}{E_\nu^2}\right] \tag{1}$$

where G_F is Fermi's coupling constant, Q_w is the weak nuclear charge, F is the ground state elastic form factor, m_t is the mass of the target nucleus, E_R is the nuclear recoil energy and E_{ν} the incident neutrino energy. $QR \lesssim 1$ is required to ensure coherence, where R is the nuclear radius. This condition can be largely satisfied when $E_{\nu} \lesssim 50 \,\text{MeV}$.

For neutrinos scattering in a target medium, the expected CE ν NS event rate can be expressed as Eq. 2, where N_t is the number of targets per unit mass, $\phi(E_{\nu})$ is the incident neutrino flux.

$$\frac{dN}{dE_R} = N_t \int \phi(E_\nu) \frac{d\sigma}{dE_R} dE_\nu \tag{2}$$

For the reactor neutrinos with energy above 2 MeV, the Huber-Mueller model[52, 53] is adopted for the spectra calculation while P. Vogel's calculation [54] is used for below 2 MeV region, which has never been experimentally explored due to the 1.8 MeV energy threshold of inverse beta decay reaction. We assume a fuel mixture of 235 U (56.1%), 238 U (7.6%), 239 Pu (30.7%), and 241 Pu (5.6%) [55], the total neutrino flux $\phi(E_{\nu})$ can be estimated with a 3 GW reactor core at 25m distance, and then the CE ν NS event rate in xenon medium can be obtained accordingly as shown in figure 5 (red). The event rate in RELICS region-of-interest (ROI) of [120, 300] PE is overlaid with (purple) and without (black) signal acceptance, respectively, which will be detailed in Sec. V.

V. BACKGROUND CONTRIBUTIONS

The complexity of the backgrounds is one of the main challenges of reactor $\text{CE}\nu\text{NS}$ detection. To overcome this

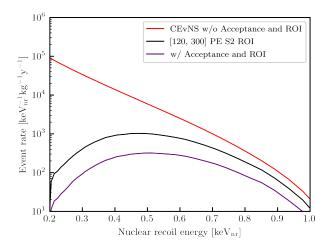


FIG. 5. The expected $\text{CE}\nu\text{NS}$ event rate in xenon medium from reactor neutrino with a flux of $10^{13}\text{cm}^{-2}\text{s}^{-1}$. The event rate in RELICS ROI of [120, 300] PE with and without signal acceptance are overlaid.

challenge, dedicated background simulations have been conducted to optimize the design of the shielding system for RELICS, using *RelicsSim* and *RelicsAPT*. The background contributions can be divided into five categories according to their origin, such as (V A) cosmic-ray neutrons, (V B) cosmic muons, (V C) detector materials, and (V D) internal background from LXe. The last one is (V E) delayed electrons, which have been observed by large LXeTPC searching for dark matter and should be treated carefully.

This section describes all the background components and is summarized in (VF). The uncertainties are due to the limited number of simulated exposures. The following criteria are applied to MC data to select the background events that can mimic $CE\nu NS$ signals:

- i. LXe-veto: The $4\pi\text{-}LXe$ veto exhibits a good background suppression because the background events are more likely to deposit energy in both active LXe and $4\pi\text{-}LXe$ veto regions. The event will be removed if it contains an NR (ER) energy larger than $500 \, (100) \, \text{keV}$ in the LXe veto region.
- ii. single-scatter: Given the small interaction cross-section of neutrino, the probability of a neutrino having more than one interaction in the sensitive LXe volume is negligible. We required that the $E_{\rm er}$ must be less than $0.05\,{\rm keV_{er}}$ in an NR event, and the second largest energy deposition of $E_{\rm er}$ less than 5% of the largest one in an ER event.
- iii. FV: Events are required to be within the center $12\,\mathrm{cm}$ radius fiducial to reduce background at the edge of the TPC, leading to a total fiducial volume (FV) of $32\,\mathrm{kg}$.
- iv. S2-width: For "S2-only" analysis, the event depth z cannot be accurately estimated. S2-width cut was

developed to remove the events around the liquidgas interface, especially for the backgrounds from detector materials.

v. In addition, dedicated selection methods are developed to suppress backgrounds out of the delayed electrons, such as waveform-classifier and pattern-classifier. These two criteria are described in detail in (VE).

A. Background induced by cosmic-ray neutrons

The cosmic rays that travel through the atmosphere can produce a variety of radiation particles, such as neutrons, protons, pions, etc., through spallation reaction on nitrogen, oxygen, etc [56, 57]. Among them, the high-energy cosmic-ray neutrons (CRNs) can easily pass through the shield and deposit energy in the RELICS detector. The main purpose of the water shield design is to block the CRNs. The size of the water tank is optimized based on the MC simulation. The CRN flux is calculated using the Cosmic-Ray Shower Generator (CRY) source [58]. Figure 6 shows the energy spectrum of the CRNs from CRY as the blue curve outside the water shield. Analyzing the MC data shows that only CRNs with energy greater than $\sim 10^3 \,\mathrm{MeV}$ can deposit energy in LXe, which indicates that the neutrons from the nuclear reactor and laboratory environment with energy less than 10 MeV [59] that also shows in figure 6, can not contribute to the backgrounds.

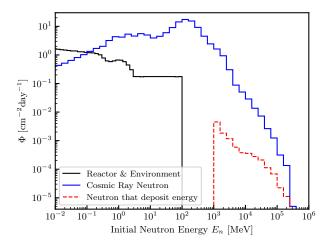
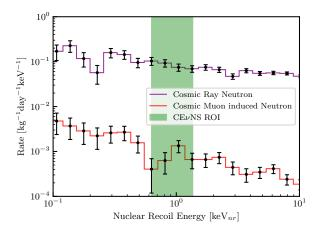


FIG. 6. The energy spectrum of the CRNs (blue) from CRY calculation. A red dashed line shows the neutrons that can deposit energy in LXe in the $\text{CE}\nu\text{NS}$ search region. The energy spectrum of the reactor and environmental neutrons from the measurement of CONUS [59] experiment is overlaid.

After processing the MC data, and passing the LXe-veto, single-scatter and FV selections, the CRNs-induced NR background rate is estimated to be $(6.0\pm0.6)\times10^{-2}\,\mathrm{kg^{-1}day^{-1}}$ in [0.63, 1.36] keV_{nr} ROI of CE ν NS searching, with the recoil energy spectrum shows

in figure 7 (top). In addition, the secondaries of CRNs will also induce ER background in LXe, with a rate of $(3.9\pm0.3)\times10^{-3}\,\mathrm{kg^{-1}day^{-1}keV^{-1}}$, which is shown in figure 7 (bottom).



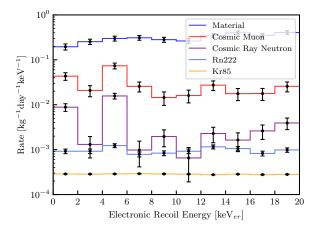


FIG. 7. Top panel: The NR background distributions from CRNs (dark magenta) and cosmic muons (red). Bottom panel: The ER background distributions from detector materials (blue), CRNs (dark magenta), cosmic muons (red), 85 Kr (sandy brown) and 222 Rn (light blue).

B. Background induced by cosmic muons

The RELICS detector will operate without overburden. Hence, special attention has to be paid to the muon-related background. Even though muons can be tagged with 99% efficiency by the PS veto detector, the neutron background produced by muon interacting with the detector materials is still one of the main background components. Dedicated simulations are performed to evaluate the muon-induced backgrounds. The energy and angular distributions of muons follow the Shukla model [60]. The energy deposition in LXe that is caused by muon-induced fast neutron and related gammas are recorded by RelicsSim, and then filtered with LXe-veto, single-scatter and FV selections. Assuming a 99% muon tag-

ging efficiency in $300\,\mu s$ veto time, the muon-induced NRs and ERs are $(0.06\pm0.01)\times10^{-2}\,\mathrm{kg^{-1}day^{-1}}$ in $[0.63,1.36]\,\mathrm{keV_{nr}}$ and $(28.0\pm2)\times10^{-3}\,\mathrm{kg^{-1}day^{-1}keV^{-1}}$ in $[0,20]\,\mathrm{keV_{er}}$, respectively. The corresponding spectra are shown in figure 7.

C. Neutrons and gammas from the detector materials

Materials constructing the detector contain radioactive contamination. The selection of the materials requires an extensive radioactivity screening campaign for rare event search experiments. The radioactive contamination for all the materials is considered in the RELICS MC model to evaluate the background contribution from these materials. Currently, the radioactivity of isotopes from XENON100 [61] is adopted. A dedicated effort is also being carried out to select clean materials for the RELICS experiment, leading to similar radioactivity for most of the materials.

The NR background rate induced by neutrons is around one event per year and completely negligible in the CE ν NS ROI. ER background induced by gammas is studied in this work. The decay of these isotopes is generated and confined uniformly in the corresponding detector component in the simulation. By applying successive selection criteria, including LXe-veto, single-scatter and FV selections, the spatial distribution of ER background events inside the active LXe volume in the energy region of $[0, 20] \text{ keV}_{er}$ is shown in figure 8. Figure 7 (bottom) shows the corresponding energy spectrum, which is more than one order of magnitude higher than other ER background components. The average ER background rate is $(310\pm10)\times10^{-3}\,\text{kg}^{-1}\text{day}^{-1}\text{keV}^{-1}$ in the FV volume.

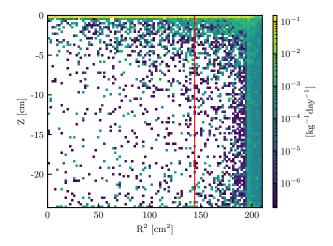


FIG. 8. Spatial distribution of ER background from detector materials inside the active LXe volume in the energy region of $[0,\ 20]$ keV $_{\rm er}$. The red line indicates the 12 cm radius fiducial selection.

S2 width selection: As shown in figure 8, a large amount of background events are located close to the

liquid-gas interface. These backgrounds are mainly from the radioactivity of PMTs and can not be suppressed with the selection in "z" in an "S2-only" analysis. However and as demonstrated in [37], the pulse shape of S2 signals can discriminate background happening at the liquid-gas interface to signals distributed uniformly in depth "z". A toy MC was conducted to consider the drift and diffusion properties of the electron clouds in LXe to optimize such a selection. We simulate S2s and their pulse shape parameters with "z" distributions shown in figure 8 with energy in the CE ν NS ROI. The S2s are simulated via RelicsAPT where the NEST model is incorporated. The S2 pulse shape is simulated using the electron diffusion model $\sigma_e = \sqrt{\frac{2D_L t}{v_d^2} + \sigma_0^2}$, where D_L is the longitudinal diffusion coefficient, v_d is the electron drift velocity, σ_0 is the width of single electron waveform [62]. In our simulation. $D_L = 16 \,\mathrm{cm}^2/\mathrm{s}, \ v_d = 0.174 \,\mathrm{cm}/\mu\mathrm{s},$ and $\sigma_0 = 0.19 \mu s$.

Uniformly distributed CE ν NS signal is simulated using the same procedure. The distributions of the S2 width are shown in figure 9, for both CE ν NS signal and ER background from the detector materials. A threshold of 0.22 μs on S2 width can give an average background rejection power of 94%, with a high CE ν NS signal acceptance of 86%.

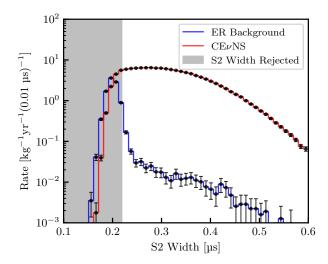


FIG. 9. The distributions of the S2 width from the uniformly distributed $\text{CE}\nu\text{NS}$ signal and ER background from detector materials. The dark region is the event that is being rejected by the S2-width criterion.

D. Internal backgrounds in LXe

Radioactivity in LXe can directly deposit energies and produce background in the CE ν NS ROI. These radioactivities mostly come in the form of noble gases, such as argon, krypton, xenon, and radon. This section describes how these radioactivities are created and evaluates their contribution to the CE ν NS ROI.

1. Intrinsic ^{222}Rn and ^{85}Kr

Krypton mixes into xenon gas when it is extracted from the air. $^{85}{\rm Kr}$, regardless of its low abundance of 2×10^{-11} in natural krypton, is one of the main backgrounds in any LXe experiments searching for rare events. The concentration of krypton in xenon is usually reduced below ppt level in dark matter search experiments, such as XENON1T and PandaX-4T, through distillations with dedicated columns [63, 64]. In RELICS, we assume a $^{nat}{\rm Kr/Xe}$ concentration of 10 ppt and expect $(0.28\pm0.01)\times10^{-3}{\rm\,kg^{-1}day^{-1}keV^{-1}}$ as shown in figure 7 (bottom), which is a subdominant component.

The other intrinsic background in LXe comes from the decays of $^{222}\mathrm{Rn}$, which emanates from any material touching xenon gas or liquid. The emanated $^{222}\mathrm{Rn}$ diffuses homogeneously inside the LXe volume within its relatively long half-life of 3.8 days. The β decay of $^{214}\mathrm{Pb}$ is another important background component in the CE ν NS ROI in the decay chain of $^{222}\mathrm{Rn}$. With similar size of TPC and materials, the radioactivity of $^{222}\mathrm{Rn}$ in RELICS is comparable to XENON100. Assuming a conservative $^{222}\mathrm{Rn}$ radioactivity of $40\,\mu\mathrm{Bq}\cdot\mathrm{kg}^{-1}$ as achieved by the XENON100 experiment [61] ($\leq 20\,\mu\mathrm{Bq}\cdot\mathrm{kg}^{-1}$), the expected ER background rate is estimated as of $(0.96\pm0.03)\times10^{-3}\,\mathrm{kg}^{-1}\mathrm{day}^{-1}\mathrm{keV}^{-1}$ as shown in figure 7 (bottom), which is also a subdominant component in the CE ν NS search.

2. Cosmogenic isotopes ¹²⁷Xe and ³⁷Ar

The RELICS experiment, which is to be operated without overburden, is inevitably exposed to cosmic radiation. We consider cosmogenic radioactive isotopes through the activation and spallation of xenon atoms. In particular, ¹²⁷Xe and ³⁷Ar are known cosmogenic backgrounds in LXeTPCs [34, 65] due to their characteristic x-rays or Auger electrons through electron capture process and their relatively long half-life of 36.4 and 35.0 days, respectively.

Natural xenon does not contain ¹²⁷Xe. ¹²⁷Xe can be produced from ¹²⁸Xe when cosmogenic muons kick off a neutron in the nucleus with a cross-section of $(2.74 \pm 0.4) \times 10^{-24}$ cm² [66]. Additionally, we consider another production channel through the neutron capture on 126Xe with an upper limit cross-section of 0.7×10^{-26} cm² at 95% C.L [66]. The production rate of ¹²⁷Xe in LXe is calculated based on its production crosssection, the muon flux [60] and thermal neutron flux [67]. The ¹²⁷Xe decays to ¹²⁷I via electron capture (EC) process, with a half-life of 36.4 days. We assume that the production and decay of ¹²⁷Xe reach equilibrium before deploying the RELICS detector inside the shielding. The estimated equilibrium decay rate is less than 9.5 atoms/day/kg. The shielding system of RELICS can attenuate neutrons efficiently, and the equilibrium decay rate can decrease to $0.79 \text{ atoms/day/kg after } \sim 300 \text{ days.}$

Following the EC, the ¹²⁷I is left primarily populating at the excited state of either 375 or 203 keV, which promptly decays to the ground state with gammaray emissions. The EC occurs from either the K, L, M, or N shell electrons and is subsequently filled with electrons from higher levels via emission of x-rays or Auger electrons with total energy (relative intensity) of 32.2 keV (83.4%), 5.2 keV (13.1%), 1.1 keV (2.9%) or 186 eV (0.7%), respectively. The final background contribution from ¹²⁷Xe is simulated with *RelicsSim*. The double-scatter criteria can remove most of these background events due to the simultaneous gamma-ray and x-ray or Auger electrons emission. If EC capture is happening from the N-shell electrons with a binding energy of 186 eV, it may contribute background in the $\text{CE}\nu\text{NS}$ ROI when the emitted gamma rays, either with energy of 375 and 203 keV, escape from the LXe detector and the active LXe veto. The event rate from 186 eV energy deposition is less than $10^{-4} \,\mathrm{kg^{-1} day^{-1}}$ after all the selection criteria described above, which is negligible for $CE\nu NS$ search.

We consider three possible mechanisms for ³⁷Ar production in xenon, following the approaches in [68]. Firstly, the extremely low content of ³⁷Ar in the atmosphere, which is generated by spallation of ⁴⁰Ar through 40 Ar(n, 4n) 37 Ar, neutron capture of 36 Ar, or cosmic bombardment of calcium-containing soils, via 40 Ca(n, α) 37 Ar. This mechanism only needs to be considered in the context of air leaks of an LXe detector, which is strictly limited to below 0.1 liter per year to ensure the purity level of LXe. Secondly, the spallation of detector materials, especially iron in steel. However, its contribution is greatly suppressed due to the slow diffusion rate of argon in steel [68]. Lastly, the direct spallation of xenon atoms by high-energy cosmogenic protons and neutrons. Only the last possibility is considered in this work. The semi-empirical formula by Silberberg and Tsao was used to calculate the spallation cross-section [69]. The CRY is used to calculate the proton spectrum. Gordon's neutron spectrum [70] is adopted for cosmogenic neutron estimation. The production rate of this process is estimated to be 0.024 atoms/kg/day with an uncertainty of $\sim 100\%$ [68]. The produced ³⁷År decays to the ground state of ³⁷Cl via EC and subsequently deposits energy via x-rays or Auger electrons. The total energy (relative intensity) for K, L, and M shells are 2.82 keV (90.2%), $0.270 \,\mathrm{keV} \,(8.9\%)$, and $0.018 \,\mathrm{keV} \,(0.9\%)$, respectively. As a results, the background rate of $^{37}\mathrm{Ar}$ in the $\mathrm{CE}\nu\mathrm{NS}$ ROI is below $10^{-4} \,\mathrm{kg^{-1} day^{-1}}$ and completely negligible for $\text{CE}\nu\text{NS}$ search.

E. Delayed electrons

Besides the background components induced by real physical sources, another type of background must be considered in the $\text{CE}\nu\text{NS}$ ROI. This background is caused by a high emission rate of delayed electrons after S2

signals in the TPC, which could be incorrectly identified as $\text{CE}\nu\text{NS}$ candidate in "S2-only" analysis. Such background has been observed by large LXeTPCs experiments searching for dark matter particles in deep underground laboratories, such as XENON1T [71], PandaX-4T [38] and LUX [72]. The source of this background is not well understood yet, but we can roughly divide the delayed electrons into two groups.

The first kind of delayed electrons is produced via photo-ionization of impurities or metals in the drift region of the TPC. Photo-ionized delay electrons only appear shortly (within a time range that is comparable to the largest drift time of the LXeTPC) after the high energy S2 signals and will be completely subdominant when a 1 ms exposure is rejected for each of the high energy S2s, leading to an exposure loss of $\simeq 1\%$.

Besides photo-ionization, delayed electrons can also be produced in a larger time range of up to a few seconds. The rate of delayed electrons is observed to be correlated with the level of impurities in LXe and the amplitude of the extraction field. Muons passing through the LXeTPC result in large energy deposition, generating a substantial number of ionization electrons. These delayed electrons may occur after the primary S2 signal of muon events, leading to a prolonged tail of signals composed of a single or a few electrons. Due to the high rate of cosmic muons, RELICS faces a major challenge in suppressing background from accidental pile-ups of delayed electrons in a short time range that is comparable to the width of a physical S2 signal. This background is hereafter referred to as Delayed Electron (DE).

1. Expected rate of DE

As shown in previous studies with XENON1T [71] and LUX [72], the emission rate of delayed electrons are correlated, in time and position, with the previous high-energy events. This part of the background is referred to as a correlated delayed electron background and can be significantly suppressed due to its unique correlation with proceeding high-energy events. We simulate muons passing through the TPC active volume using Geant4, tracking their interaction vertex and the energy deposited along the track. The ionization signals are generated along the muon track, assuming a constant ionization yield of 50 electrons per keV. We then simulated the generation of delayed electrons, assuming that 0.1% of the total ionization electrons from primary interactions are delayed emissions in a time range of 0.1 ms to 2 s, comparable to [71]. The distribution in "delayed time" (time with respect to the primary S2) for delayed electrons is assumed to follow a power law with a coefficient of -1.1, as shown in XENON1T [71]. These delayed electrons' horizontal positions (x, y) are assumed to be the same as their primary S2s. Position reconstruction resolution for single electron S2s, which is expected to be 20 mm from optical simulations, is taken into account in this analysis. Ionization S2 signals are grouped together if the time gap between them is below $1\,\mu s$ in order not to split S2 waveforms of events happening at the bottom part of the TPC. As a result, the pile-up of DE (called Pile-up DEs) leads to a significant background in CE ν NS search. In RELICS, we expect more than 10 Hz of muon events in the LXeTPC, leaving a large amount of single electron S2 signals. The expected event rate of a single-electron pile-up background is summarized in Tab. II. Without implementing appropriate cuts to reduce the rate of these pile-up events, CE ν NS signals with 3 to 6 electrons will be completely overwhelmed.

TABLE II. A comparison of the $\text{CE}\nu\text{NS}$ signal and the Pile-up DEs background in one year of exposure with 32 kg of fiducial mass.

N_e	$\text{CE}\nu \text{NS}$	Pile-up DEs
3	2.4×10^4	9.8×10^{8}
4	1.1×10^4	7.3×10^{6}
5	5.2×10^3	6.9×10^{5}
6	2.4×10^{3}	7.5×10^4

2. Waveform classifier

The waveform characteristics of Pile-up DE events differ from the physical interactions in the LXeTPC, such as $CE\nu NS$ and other backgrounds. In physical interactions, electrons drift upwards under the drifting electric field, resulting in signal waveform distributions that follow a Gaussian distribution in time. As shown in figure 10, Pile-up DEs are distinguishable from physical interactions in terms of the shape of waveforms. The discrimination between them is maximized by employing a convolutional neural network (CNN), as shown in figure 11. While maintaining $\sim 80\%$ of the physical interactions with a score over 0.8, the Pile-up DE events are reduced by approximately one order of magnitude.

3. Pattern classifier

Beyond the distinctions in time distribution of the waveform, the planar distribution of signals within the top PMT arrays also presents notable differences between Pile-up DE and physical interactions. $CE\nu NS$ and other physical signals are composed of multiple electrons generated from the same position below the liquid surface in the detector, while the DE signals are mostly generated around the previous muons' tracks. These DEs are merged together into larger signals only due to their temporal proximity. Therefore, the distributions of photoelectrons from $CE\nu NS$ signals and DE signals differ in the top PMT array of the detector. Real physical interactions appear more like a superposition of multiple single-electron signals from the same location, whereas the Pile-

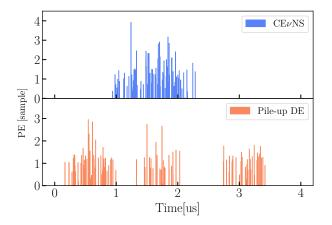


FIG. 10. Simulated waveform of Pile-up DE and $\text{CE}\nu\text{NS}$. Recording the number of photo-electrons collected for each sample, the upper panel corresponds to real physical events, and the lower panel represents the Pile-up DE events.

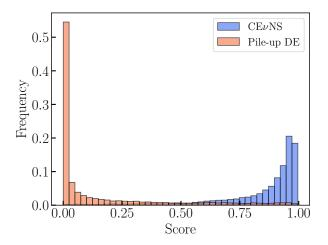


FIG. 11. Result of waveform discrimination by CNN. The waveform is evaluated by CNN, which provides predicted scores indicating the discriminability between the two types of waveform.

up DEs are formed by the superposition of single-electron signals originating from multiple different horizontal positions, thus appearing more dispersed.

For an $\text{CE}\nu\text{NS}$ or physical interaction, the expected photo-electrons detected in each channel on the top PMT array are denoted as λ_{ch} . λ_{ch} is determined by the total area of S2, the relative LCE in that channel, and the PMT responses including detection efficiency. LCE of each PMT is derived with light propagation simulation in the RELICS TPC. It is assumed that the number of photo-electrons received by the PMT channel follows a Poisson distribution with λ_{ch} as the mean. The detected photo-electrons are further derived considering the resolution of PMTs to a single photo-electron.

While the "expected" λ_{ch} is simulated with multiple electrons generated from the same position, the "ob-

served" photo-electrons N_{ch}^{pe} in each channel from an "unknown" event is calculated by summing up the simulation from each electron at its corresponding position. Given the expected and observed distribution pattern, we calculated the goodness-of-fit likelihood to determine whether the event is from physical interactions or Pile-up DEs. The logarithm of goodness-of-fit likelihood P is written as:

$$P = \sum_{ch=0}^{63} \log \left(\frac{\lambda_{ch}^{N_{ch}^{pe}} \times e^{-\lambda_{ch}}}{N_{ch}^{pe}!} \right)$$
(3)

The S2 distribution pattern on top PMT array of the Pile-up DEs rejected by a selection in P (figure 12, top) would look like that of physical interactions (figure 12, bottom). Since both the horizontal position and emission time of DEs are strongly correlated to the previous muon tracks, we further calculate the "Space-time Correlation Coefficient" of each event to prior muons to distinguish Pileup DEs from physical interactions that are independent of any muon events in the RELICS LXeTPC.

For each energy deposition of muon passing through the RELICS TPC, the reconstructed position of DEs would follow a Gaussian distribution determined by the resolution of position reconstruction. The distribution of DEs in time with respect to the previous muon events is assumed to follow a power law, as seen in [71]. Assuming N_i is the expected number of DE in a specific position, the probability distribution function of DEs can be expressed as:

$$P_i = N_i \times (t - t_i)^{-\gamma} \times \frac{1}{2\pi \cdot \sigma^2} e^{-\frac{(x - x_i)^2 + (y - y_i)^2}{2\sigma^2}}$$
 (4)

where (x_i, y_i) is the position of muon track, (x, y) is the observed position, $t - t_i$ is the time delay to the muon track and σ is the resolution of reconstructed position. Considering that the emission of DE can last up to \simeq 2s and the muon event rate of \simeq 10 Hz, we sum up the contributions of P_i from the previous 20 muons and define the log of this value as the "Space-time Coefficient", which is defined as:

$$C_{Space-time} = \log\left(\sum_{i} P_{i}\right)$$
 (5)

We simulated the Pile-up DE events of the detector operating for 8500 hours and calculated the "Pattern coefficient" P and "Spacetime Correlation Coefficient" $C_{Space-time}$ for each event. The event distribution in $(P, C_{Space-time})$ space slightly varies with different S2 sizes. To clearly illustrate the discrimination power, the Pile-up DE and $\text{CE}\nu\text{NS}$ events in the energy slice of [150, 160] PEs in the $(P, C_{Space-time})$ space are shown in figure 13.

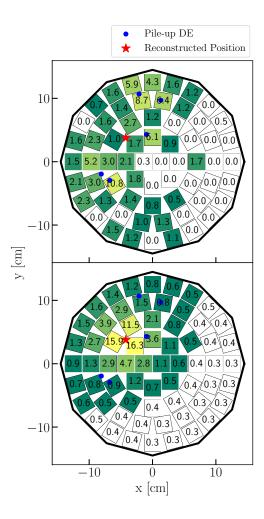


FIG. 12. The observed S2 pattern (N_{ch}^{pe}) on top PMT array from one Pile-up DE event (top) and the expected pattern (λ_{ch}) from the corresponding reconstructed position (bottom) with the same S2 area from physical interaction. Expected PE numbers for each channel are provided. Only channels with an expected area greater than 0.5 PE are shown with color.

Considering the correlation between $C_{Space-time}$, P and the S2 area of each event, we provide a score for each event by Eq. 6. Events with higher scores are inclined to be from physical interactions.

$$Score = P - (k_{st} \cdot C_{space-time}) + k_{area} \cdot S2_{area} + b$$
 (6)

While restricting the acceptance of Pile-up DE events lower than 0.005%, we scanned the parameter space of k_{st} and k_{area} , in order to retain as high signal acceptance as possible. The fitted values are k_{st} of 5.6 , k_{area} of 0.8 and b of -37.42.

Figure 14 delineates the score distribution for Pile-up DEs and physical interactions. The final classifier identifies all events with scores exceeding 0 as real physical interactions. In the ROI of S2 ranging from 120 to 300 PE, the acceptance for physical interactions such as $\text{CE}\nu\text{NS}$

is 46.5%. This cut reduced the rate of Pile-up DEs by 4 orders of magnitude in the same ROI, leaving the rate of Pile-up DE background below the expected $\text{CE}\nu\text{NS}$ signal in the whole ROI.

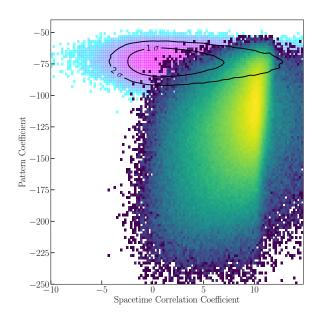


FIG. 13. Distribution of pattern likelihood and space-time correlation of Pile-up DE and CE ν NS S2 signals with S2 area range from 150 to 160 PE. CE ν NS events are represented by green/yellow points and Pile-up DE events are represented by blue/violet points. Contours of CE ν NS events distribution are also overlaid.

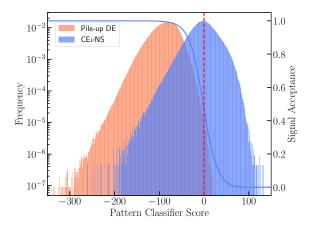


FIG. 14. Distribution of scores from pattern classifier. The survival rate for CE ν NS within ROI with scores over 0 is 46.5% and 0.005% for Pile-up DE events within ROI.

F. Summary

Considering the correlations between S2-width, waveform-classifier and pattern-classifier criteria, the total acceptance of these three cuts is estimated as shown in figure 15.

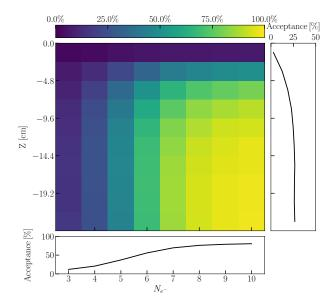


FIG. 15. The acceptance of $\text{CE}\nu\text{NS}$ signals by applying the event selection criteria of S2-width, waveform-classifier and pattern-classifier, in-depth "z" vs number of electrons N_{e^-} space.

The distribution of all the background components is converted to S2 size in photo-electrons from recoil energy using RelicsAPT, which is described in Sec. III, and summarized in figure 16. The $CE\nu NS$ event rate is overlaid taking into account the signal acceptance. The dominant background contribution comes from the Pile-up DEs, despite its large discrimination power to physical events as described in Sec. V E. The NR background contribution from CRNs is the second major contribution. The detector materials contribute a relatively low and flat component in ER. The background components' event rate in $32\,\mathrm{kg}$ -yr exposure is summarized in Tab. III.

While not utilized for our baseline sensitivity, we are aware that the reactor-OFF period can be used to further constrain our background model [73, 74]. Since the reactor-related background is negligible in the total budget, this data will provide a background-only measurement and dedicated runs can be planned in the future to enhance the signal sensitivity.

VI. PHYSICS POTENTIAL

To explore the physics potential of the RELICS detector, this section will discuss its sensitivity to the weak mixing angle and non-standard interactions (NSI) with

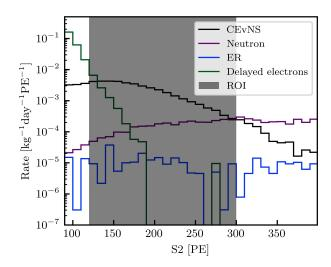


FIG. 16. Expected S2 distribution of $\text{CE}\nu\text{NS}$ (Black) signal among all background contributions in the RELICS experiment. The dominant background is the Pile-up DE (Green) induced by muons in the TPC. The second largest background is neutrons (Purple), mainly from the CRNs. The ER from radioactivity of detector material, CRNs, and muons (Blue) is a non-dominant background. The ROI for the $\text{CE}\nu\text{NS}$ search is defined as 120 PE to 300 PE, denoted as the shaded region.

TABLE III. The total number of expected events ($N_{\rm evts}$) of all the background components in [120, 300] PE ROI of $CE\nu NS$ detection in 32 kg·yr exposure.

Event Type	N_{evts}
Pile-up DE	1325.1
CRNs	339.9
Muon-induced neutrons	1.7
ER	21.1
Total Background	1687.8
$\text{CE}\nu \text{NS}$	4639.7

neutrino has vector couplings to the up and down quarks based on the background estimation in section V with 32 kg·yr exposure. Several systematic uncertainties are considered, including 5% reactor neutrino flux, 10% ER and 5% NR background uncertainty. The uncertainty of the Q_y introduced in Sec. III A is the dominant one in our estimation.

A. Weak mixing angle

A precise measurement of $\text{CE}\nu\text{NS}$ cross-section allows for a constraint on the weak mixing angle $\theta_{\rm w}$. Also known as the Weinberg angle, $\theta_{\rm w}$ is conventionally used in the form of $\sin^2\theta_{\rm w}$ in the comparison between theory and experiment. Since Q_w is given by $N-\left(1-4\sin^2\theta_{\rm w}\right)Z$, $\sin^2\theta_{\rm w}$ can be extracted from the measured cross-section, and any deviation from the SM prediction will indicate new physics.

TABLE IV. List of nuisance parameters shared in the likelihoods for measuring the weak mixing angle and searching for NSI. All the nuisance parameters are constrained by Gaussian distribution, and their standard deviations (constraints) are also listed in the table.

Nuisance Parameters	Constraints	
Charge yield morpher	t	1 [44]
Reactor neutrino flux multiplier	γ_f	$ \begin{aligned} \sigma_{\gamma_f} &= 0.05 \\ \sigma_{\beta_1} &= 0.10 \end{aligned} $
ER background rate multiplier	β_1	$\sigma_{\beta_1} = 0.10$
Neutron background rate multiplier	β_2	$\sigma_{\beta_2} = 0.05$
Pile-up DE background rate multiplier	β_3	$\sigma_{\beta_3} = 0.10$

$$\chi^{2} = \sum_{j} \left[\frac{\left(N_{\text{obs},j} - N_{\text{exp},j} (\sin^{2} \theta_{W}, t) (1 + \gamma_{f}) - \sum_{i}^{3} B_{i,j} (1 + \beta_{i}) \right)^{2}}{\sigma_{\text{stat},j}^{2}} \right] + t^{2} + \sum_{i}^{3} \left(\frac{\beta_{i}}{\sigma_{\beta_{i}}^{2}} \right)^{2} + \left(\frac{\gamma_{f}}{\sigma_{\gamma_{f}}^{2}} \right)^{2}$$
(7)

The χ^2 of likelihood for $\sin^2\theta_w$ measurement is defined as Eq. 7 where index j indicates different S2 intervals. $N_{\text{obs},j}$ and $N_{\exp,j}$ are the observed and expected signal events in each S2 interval, respectively. $B_{i,j}$ is the background rate estimation and index i runs over background components, including ER and neutrons. The rest are nuisance parameters. β_1 , β_2 and β_3 are the multipliers of the ER, neutron and Pile-up DE backgrounds, respectively. t denotes the morphers of charge yields. A Gaussian constraint term is imposed on each nuisance parameter, as summarized in Tab. IV.

The expected constraint on $\sin^2\theta_{\rm w}$ from RELICS is shown in figure 17. The great improvement from the red solid line to the blue dashed line indicates that the charge yield variation is a major contribution to the constraint uncertainty. The sensitivity is expected to be competitive and improve the Dresden-II's result [75] measured with reactor neutrinos. As illustrated in figure 18, RELICS will provide a measurement on $\sin^2\theta_w$ with momentum transfer down to the MeV scale, which is a valuable complement to the current measurements.

B. Nonstandard neutrino interactions

The detection of CE ν NS provides a new probe to study neutrino physics beyond the SM, such as the NSI of neutrinos. NSI has been extensively studied in the literature [81]. This work focuses on a model-independent approach in the neutrino-quark sector. The parameterization of the NSI contributions to the cross-section can be expressed as Eq. 8, which indicates that the cross-section strongly depends on the effective electron neutrino-up quark and -down quark interaction strength parameters of ϵ_{ee}^{UV} and ϵ_{ee}^{dV} .

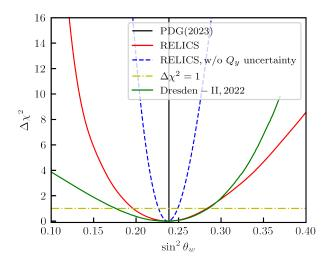


FIG. 17. The expected constraints on $\sin^2 \theta_w$ with RELICS. The red line shows the nominal likelihood curve defined by χ^2 in Eq. 7, while the blue dashed line illustrates the likelihood curve with the charge yield fixed. The faint green dot-dashed line marks $\Delta \chi^2 = 1$, and its intersections with each likelihood curve represent the constraint. The Dresden-II result (green) [75] and the PDG value (black) [76] are overlaid for reference.

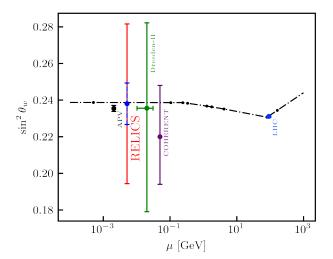


FIG. 18. The expected measurement (red) on $\sin^2 \theta_w$ with RELICS. The result without Q_y uncertainty is overlaid with a blue-dashed error bar. The black line represents the dependence of the weak mixing angle in the $\overline{\rm MS}$ renormalization scheme [77]. A comparison with experimental measurements from COHERENT [78], Dresden-II [75], atomic parity violation (APV) [79], and LHC [80] are also shown.

$$\begin{split} \frac{d\sigma}{dE_R} = & \frac{G_F^2 \cdot m_t}{2\pi} F^2 \left(2m_t E_R\right) \left[2 - \frac{m_t E_R}{E_\nu^2}\right] \\ & \times \left[Z(g_V^p + 2\epsilon_{ee}^{uV} + \epsilon_{ee}^{dV}) + N(g_V^n + \epsilon_{ee}^{uV} + 2\epsilon_{ee}^{dV})\right]^2 \end{split} \tag{8}$$

Eq.9 defines the χ^2 of likelihood, where all the parameters are the same as Eq.7, except ϵ_{ee}^{uV} and ϵ_{ee}^{dV} . All

the related uncertainties of nuisance parameters are also taken in Tab. IV. Figure 19 shows the constraining on ϵ_{ee}^{uV} and ϵ_{ee}^{dV} of RELICS under the standard model assumption, where both of the parameters are zero. The latest result from COHERENT [78] is overlaid for comparison. A tighter constraint can be achieved for the RELICS experiment with higher statistics.

$$\chi^{2} = \sum_{j} \left[\frac{\left(N_{\text{obs},j} - N_{\text{exp},j} (\epsilon_{ee}^{uV}, \epsilon_{ee}^{dV}, t) (1 + \gamma_{f}) - \sum_{i}^{3} B_{i,j} (1 + \beta_{i}) \right)^{2}}{\sigma_{\text{stat},j}^{2}} \right] + t^{2} + \sum_{i}^{3} \left(\frac{\beta_{i}}{\sigma_{\beta_{i}}^{2}} \right)^{2} + \left(\frac{\gamma_{f}}{\sigma_{\gamma_{f}}^{2}} \right)^{2}$$

$$(9)$$

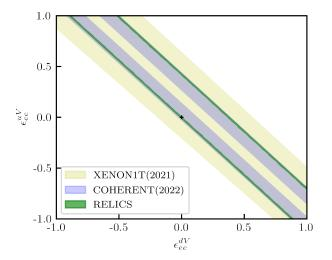


FIG. 19. The 90% allowed parameter space of $(\epsilon_{ee}^{uV}, \epsilon_{ee}^{dV})$ constrained by RELICS detector. The COHERENT [78] and XENON1T [44] results are superimposed for comparison.

VII. SUMMARY

The RELICS experiment is a $\mathcal{O}(100)$ kg LXe detector with a fiducial mass of 32 kg that aims to observe the process of reactor CE ν NS. The experiment is planned to be deployed at the Sanmen Nuclear Power Plant (~ 3 GW) in Zhejiang province, China, with a distance of ~ 25 m, an average neutrino flux of $\sim 10^{13}$ cm⁻²s⁻¹.

In this work, a preliminary design of the RELICS experiment was presented. A dedicated MC simulation has been performed to study the background contributions. The dominant backgrounds come from the Pile-up DEs. The second largest background, nuclear recoils induced by cosmic-ray neutrons, is suppressed via a passive water shield. An ionization-only analysis channel will be adopted for RELICS analysis to achieve a sufficiently low energy threshold for $\text{CE}\nu\text{NS}$ detection. Its sensitivity to weak mixing angle and neutrino NSI are explored with $32\,\text{kg}\cdot\text{yr}$ exposure.

The RELICS experiment will provide rich opportunities to study Beyond the Standard Model (BSM) physics and potential applications in nuclear reactor monitoring for nuclear safeguards.

Acknowledgements. We acknowledge CNNC Sanmen Nuclear Power Company for hosting RELICS. We thank Dr. Xun Chen for supporting the BambooMC package and Prof. Kaixuan Ni for fruitful discussions. RELICS is supported by a National Key R&D grant from the Ministry of Science and Technology of China (No. 2021YFA1601600), a grant from the Natural Science Foundation of China (No. 12275267) and the Fundamental Research Funds for the Central Universities, Sun Yat-sen University (No. 22lglj11). Yifei Zhao's work on RELICS is supported by a grant for undergraduate research from Beijing Natural Science Foundation (No. QY23088).

D. Z. Freedman, Coherent effects of a weak neutral current, Phys. Rev. D 9, 1389 (1974).

^[2] D. Akimov et al. (COHERENT), Observation of Coherent Elastic Neutrino-Nucleus Scattering, Science 357, 1123 (2017), arXiv:1708.01294 [nucl-ex].

^[3] D. Akimov et al. (COHERENT), First Measurement of Coherent Elastic Neutrino-Nucleus Scattering on Argon, Phys. Rev. Lett. 126, 012002 (2021), arXiv:2003.10630 [nucl-ex].

^[4] B. C. Cañas, E. A. Garcés, O. G. Miranda, and A. Parada, Future perspectives for a weak mixing angle measurement in coherent elastic neutrino nucleus scattering experiments, Phys. Lett. B 784, 159 (2018), arXiv:1806.01310 [hep-ph].

^[5] J. Barranco, O. G. Miranda, and T. I. Rashba, Low energy neutrino experiments sensitivity to physics beyond the Standard Model, Phys. Rev. D 76, 073008 (2007), arXiv:hep-ph/0702175.

^[6] A. J. Anderson, J. M. Conrad, E. Figueroa-Feliciano, C. Ignarra, G. Karagiorgi, K. Scholberg, M. H. Shaevitz, and J. Spitz, Measuring Active-to-Sterile Neutrino Oscillations with Neutral Current Coherent Neutrino-Nucleus Scattering, Phys. Rev. D 86, 013004 (2012), arXiv:1201.3805 [hep-ph].

^[7] A. C. Dodd, E. Papageorgiu, and S. Ranfone, The Effect of a neutrino magnetic moment on nuclear excitation processes, Phys. Lett. B 266, 434 (1991).

^[8] K. Patton, J. Engel, G. C. McLaughlin, and N. Schunck, Neutrino-nucleus coherent scattering as a probe of neutron density distributions, Phys. Rev. C 86, 024612 (2012), arXiv:1207.0693 [nucl-th].

^[9] A. M. Suliga, J. F. Beacom, and I. Tamborra, Towards probing the diffuse supernova neutrino background in all flavors, Phys. Rev. D 105, 043008 (2022), arXiv:2112.09168 [astro-ph.HE].

^[10] A. Abdukerim et al. (PandaX), PandaX-xT: a Multi-

- ten-tonne Liquid Xenon Observatory at the China Jinping Underground Laboratory, (2024), arXiv:2402.03596 [hep-ex].
- [11] J. Aalbers et al., A next-generation liquid xenon observatory for dark matter and neutrino physics, J. Phys. G 50, 013001 (2023), arXiv:2203.02309 [physics.ins-det].
- [12] E. Aprile et al. (XENON), First Measurement of Solar ⁸B Neutrinos via Coherent Elastic Neutrino-Nucleus Scattering with XENONnT, (2024), arXiv:2408.02877 [nuclex].
- [13] Z. Bo et al. (PandaX), First Measurement of Solar ⁸B Neutrino Flux through Coherent Elastic Neutrino-Nucleus Scattering in PandaX-4T, (2024), arXiv:2407.10892 [hep-ex].
- [14] J. Billard, L. Strigari, and E. Figueroa-Feliciano, Implication of neutrino backgrounds on the reach of next generation dark matter direct detection experiments, Phys. Rev. D 89, 023524 (2014), arXiv:1307.5458 [hep-ph].
- [15] C. A. J. O'Hare, New Definition of the Neutrino Floor for Direct Dark Matter Searches, Phys. Rev. Lett. 127, 251802 (2021), arXiv:2109.03116 [hep-ph].
- [16] J. Tang and B.-L. Zhang, Dark matter, $\text{CE}\nu \text{NS}$ and neutrino new physics scrutinized by a statistical method in Xenon-based experiments, (2024), arXiv:2403.05819 [hep-ph].
- [17] J. Colaresi, J. I. Collar, T. W. Hossbach, C. M. Lewis, and K. M. Yocum, Measurement of Coherent Elastic Neutrino-Nucleus Scattering from Reactor Antineutrinos, Phys. Rev. Lett. 129, 211802 (2022), arXiv:2202.09672 [hep-ex].
- [18] H. Bonet *et al.* (CONUS), Constraints on elastic neutrino nucleus scattering in the fully coherent regime from the CONUS experiment, Phys. Rev. Lett. **126**, 041804 (2021), arXiv:2011.00210 [hep-ex].
- [19] A. Aguilar-Arevalo et al. (CONNIE), Search for coherent elastic neutrino-nucleus scattering at a nuclear reactor with CONNIE 2019 data, JHEP 05, 017, arXiv:2110.13033 [hep-ex].
- [20] D. Y. Akimov et al. (RED-100), First ground-level laboratory test of the two-phase xenon emission detector RED-100, JINST 15 (02), P02020, arXiv:1910.06190 [physics.ins-det].
- [21] K. Ni, J. Qi, E. Shockley, and Y. Wei, Sensitivity of a Liquid Xenon Detector to Neutrino-Nucleus Coherent Scattering and Neutrino Magnetic Moment from Reactor Neutrinos, Universe 7, 54 (2021).
- [22] G. Agnolet et al. (MINER), Background Studies for the MINER Coherent Neutrino Scattering Reactor Experiment, Nucl. Instrum. Meth. A 853, 53 (2017), arXiv:1609.02066 [physics.ins-det].
- [23] G. Angloher *et al.* (NUCLEUS), Exploring CEνNS with NUCLEUS at the Chooz nuclear power plant, Eur. Phys. J. C **79**, 1018 (2019), arXiv:1905.10258 [physics.ins-det].
- [24] I. Alekseev *et al.* (ν GeN), First results of the ν GeN experiment on coherent elastic neutrino-nucleus scattering, Phys. Rev. D **106**, L051101 (2022), arXiv:2205.04305 [nucl-ex].
- [25] S. Karmakar, M. K. Singh, H. T. Wong, H. B. Li, V. Sharma, G. C., M. K. Singh, and F. K. Lin (TEX-ONO), Constraints on the coherent elastic neutrino nucleus scattering from reactor neutrinos at TEXONO experiment, DAE Symp. Nucl. Phys. 67, 1167 (2024).
- [26] G. Fernandez-Moroni, R. Harnik, P. A. N. Machado, I. Martinez-Soler, Y. F. Perez-Gonzalez, D. Rodrigues,

- and S. Rosauro-Alcaraz, The physics potential of a reactor neutrino experiment with Skipper-CCDs: searching for new physics with light mediators, JHEP **02**, 127, arXiv:2108.07310 [hep-ph].
- [27] C. Augier et al. (Ricochet), Ricochet Progress and Status, J. Low Temp. Phys. 212, 127 (2023), arXiv:2111.06745 [physics.ins-det].
- [28] E. P. Bernard et al., Thermodynamic stability of xenon-doped liquid argon detectors, Phys. Rev. C 108, 045503 (2023), arXiv:2209.05435 [physics.ins-det].
- [29] M. Lindner, W. Rodejohann, and X.-J. Xu, Coherent Neutrino-Nucleus Scattering and new Neutrino Interactions, JHEP 03, 097, arXiv:1612.04150 [hep-ph].
- [30] D. K. Papoulias, T. S. Kosmas, and Y. Kuno, Recent probes of standard and non-standard neutrino physics with nuclei, Front. in Phys. 7, 191 (2019), arXiv:1911.00916 [hep-ph].
- [31] C. von Raesfeld and P. Huber, Use of CEvNS to monitor spent nuclear fuel, Phys. Rev. D 105, 056002 (2022), arXiv:2111.15398 [hep-ph].
- [32] Y. Meng et al. (PandaX-4T), Dark Matter Search Results from the PandaX-4T Commissioning Run, Phys. Rev. Lett. 127, 261802 (2021), arXiv:2107.13438 [hep-ex].
- [33] E. Aprile et al. (XENON), Search for New Physics in Electronic Recoil Data from XENONnT, Phys. Rev. Lett. 129, 161805 (2022), arXiv:2207.11330 [hep-ex].
- [34] J. Aalbers et al. (LZ), First Dark Matter Search Results from the LUX-ZEPLIN (LZ) Experiment, Phys. Rev. Lett. 131, 041002 (2023), arXiv:2207.03764 [hep-ex].
- [35] G. Adhikari et al. (nEXO), nEXO: neutrinoless double beta decay search beyond 10²⁸ year half-life sensitivity, J. Phys. G 49, 015104 (2022), arXiv:2106.16243 [nucl-ex].
- [36] G. Anton *et al.* (EXO-200), Search for Neutrinoless Double- β Decay with the Complete EXO-200 Dataset, Phys. Rev. Lett. **123**, 161802 (2019), arXiv:1906.02723 [hep-ex].
- [37] E. Aprile et al. (XENON), Light Dark Matter Search with Ionization Signals in XENON1T, Phys. Rev. Lett. 123, 251801 (2019), arXiv:1907.11485 [hep-ex].
- [38] S. Li et al. (PandaX), Search for Light Dark Matter with Ionization Signals in the PandaX-4T Experiment, Phys. Rev. Lett. 130, 261001 (2023), arXiv:2212.10067 [hep-ex].
- [39] E. Aprile et al. (XENON), Design and Performance of the XENON10 Dark Matter Experiment, Astropart. Phys. 34, 679 (2011), arXiv:1001.2834 [astro-ph.IM].
- [40] X. Chen et al., BambooMC A Geant4-based simulation program for the PandaX experiments, JINST 16 (09), T09004, arXiv:2107.05935 [physics.ins-det].
- [41] D. Xu, Z. Xu, J. R. Angevaare, and L. Hoetzsch, Xenonnt/appletree: v0.3.0 (2023).
- [42] E. Aprile *et al.* (XENON), The XENONnT Dark Matter Experiment, (2024), arXiv:2402.10446 [physics.ins-det].
- [43] M. Szydagis, J. Balajthy, G. A. Block, J. P. Brodsky, E. Brown, J. E. Cutter, S. J. Farrell, J. Huang, E. S. Kozlova, C. S. Liebenthal, A. Manalaysay, D. N. McKinsey, K. McMichael, M. Mooney, J. Mueller, K. Ni, G. R. C. Rischbieter, M. Tripathi, C. D. Tunnell, V. Velan, M. D. Wyman, Z. Zhao, and M. Zhong, A Review of NEST Models, and Their Application to Improvement of Particle Identification in Liquid Xenon Experiments (2022), arXiv:2211.10726 [astro-ph, physics:hep-ex, physics:nuclex, physics:physics].
- [44] E. Aprile et al. (XENON), Search for Coherent Elastic

- Scattering of Solar ⁸B Neutrinos in the XENON1T Dark Matter Experiment, Phys. Rev. Lett. **126**, 091301 (2021), arXiv:2012.02846 [hep-ex].
- [45] D. S. Akerib et al. (LUX), Technical Results from the Surface Run of the LUX Dark Matter Experiment, Astropart. Phys. 45, 34 (2013), arXiv:1210.4569 [astroph.IM].
- [46] G. M. Seidel, R. E. Lanou, and W. Yao, Rayleigh scattering in rare gas liquids, Nucl. Instrum. Meth. A 489, 189 (2002), arXiv:hep-ex/0111054.
- [47] A. Baldini et al., Absorption of scintillation light in a 100 l liquid xenon gamma ray detector and expected detector performance, Nucl. Instrum. Meth. A 545, 753 (2005), arXiv:physics/0407033.
- [48] S. Bricola, A. Menegolli, M. Prata, M. C. Prata, G. L. Raselli, M. Rossella, and C. Vignoli, Noble-gas liquid detectors: Measurement of light diffusion and reflectivity on commonly adopted inner surface materials, Nucl. Phys. B Proc. Suppl. 172, 260 (2007).
- [49] Hamamatsu inc., private communications.
- [50] C. H. Faham, V. M. Gehman, A. Currie, A. Dobi, P. Sorensen, and R. J. Gaitskell, Measurements of wavelength-dependent double photoelectron emission from single photons in VUV-sensitive photomultiplier tubes, JINST 10 (09), P09010, arXiv:1506.08748 [physics.ins-det].
- [51] B. López Paredes, H. M. Araújo, F. Froborg, N. Marangou, I. Olcina, T. J. Sumner, R. Taylor, A. Tomás, and A. Vacheret, Response of photomultiplier tubes to xenon scintillation light, Astropart. Phys. 102, 56 (2018), arXiv:1801.01597 [physics.ins-det].
- [52] P. Huber, On the determination of anti-neutrino spectra from nuclear reactors, Phys. Rev. C 84, 024617 (2011), [Erratum: Phys.Rev.C 85, 029901 (2012)], arXiv:1106.0687 [hep-ph].
- [53] T. A. Mueller et al., Improved Predictions of Reactor Antineutrino Spectra, Phys. Rev. C 83, 054615 (2011), arXiv:1101.2663 [hep-ex].
- [54] P. Vogel, G. K. Schenter, F. M. Mann, and R. E. Schenter, Reactor Anti-neutrino Spectra and Their Application to Anti-neutrino Induced Reactions. 2., Phys. Rev. C 24, 1543 (1981).
- [55] A. Abusleme et al. (JUNO), TAO Conceptual Design Report: A Precision Measurement of the Reactor Antineutrino Spectrum with Sub-percent Energy Resolution, (2020), arXiv:2005.08745 [physics.ins-det].
- [56] H. Liu, Y. Hou, H. Li, Y. Song, L. Hu, and M. Liang, Cosmic-ray neutron fluxes and spectra at different altitudes based on Monte Carlo simulations, Appl. Radiat. Isot. 175, 109800 (2021).
- [57] M. Becchetti et al., Measurements and simulations of the cosmic-ray-induced neutron background, Nucl. Instrum. Meth. A 777, 1 (2015).
- [58] C. Hagmann, D. Lange, and D. Wright, Cosmic-ray shower generator (CRY) for Monte Carlo transport codes (2007).
- [59] J. Hakenmüller et al., Neutron-induced background in the CONUS experiment, Eur. Phys. J. C 79, 699 (2019), arXiv:1903.09269 [physics.ins-det].
- [60] P. Shukla and S. Sankrith, Energy and angular distributions of atmospheric muons at the Earth, Int. J. Mod. Phys. A 33, 1850175 (2018), arXiv:1606.06907 [hep-ph].
- [61] E. Aprile et al. (XENON100), Study of the electromagnetic background in the XENON100 experiment, Phys.

- Rev. D **83**, 082001 (2011), [Erratum: Phys.Rev.D 85, 029904 (2012)], arXiv:1101.3866 [astro-ph.IM].
- [62] P. Sorensen, Anisotropic diffusion of electrons in liquid xenon with application to improving the sensitivity of direct dark matter searches, Nucl. Instrum. Meth. A 635, 41 (2011), arXiv:1102.2865 [astro-ph.IM].
- [63] E. Aprile et al. (XENON), Removing krypton from xenon by cryogenic distillation to the ppq level, Eur. Phys. J. C 77, 275 (2017), arXiv:1612.04284 [physics.ins-det].
- [64] R. Yan et al., PandaX-4T cryogenic distillation system for removing krypton from xenon, Rev. Sci. Instrum. 92, 123303 (2021), arXiv:2107.09398 [physics.ins-det].
- [65] X. Cui et al. (PandaX-II), Dark Matter Results From 54-Ton-Day Exposure of PandaX-II Experiment, Phys. Rev. Lett. 119, 181302 (2017), arXiv:1708.06917 [astro-ph.CO].
- [66] Y. M. Gavrilyuk, A. M. Gangapshev, V. V. Kazalov, V. V. Kuzminov, S. I. Panasenko, S. S. Ratkevich, D. A. Tekueva, and S. P. Yakimenko, The origin of the background radioactive isotope ¹²⁷Xe in the sample of Xe enriched in ¹²⁴Xe, Phys. Part. Nucl. 48, 42 (2017), arXiv:1507.04181 [nucl-ex].
- [67] K. Munehiko et al., Evaluation of Geomagnetic Latitude Dependence of the Cosmic-ray Induced Environmental Neutrons in Japan, Journal of NUCLEAR SCIENCE and TECHNOLOGY 44, 114–120 (2007).
- [68] J. Aalbers et al. (LZ), Cosmogenic production of Ar37 in the context of the LUX-ZEPLIN experiment, Phys. Rev. D 105, 082004 (2022), arXiv:2201.02858 [hep-ex].
- [69] R. Silberberg and C. H. Tsao, Partial Cross-Sections in High-Energy Nuclear Reactions, and Astrophysical Applications. I. Targets With z <= 28., Astrophys. J. Suppl. 25, 315 (1973).
- [70] M. S. Gordon, P. Goldhagen, K. P. Rodbell, T. H. Zabel, H. H. K. Tang, J. M. Clem, and P. Bailey, Measurement of the flux and energy spectrum of cosmic-ray induced neutrons on the ground, IEEE Trans. Nucl. Sci. 51, 3427 (2004).
- [71] E. Aprile et al. (XENON), Emission of single and few electrons in XENON1T and limits on light dark matter, Phys. Rev. D 106, 022001 (2022), arXiv:2112.12116 [hepex].
- [72] D. S. Akerib et al. (LUX), Investigation of background electron emission in the LUX detector, Phys. Rev. D 102, 092004 (2020), arXiv:2004.07791 [physics.ins-det].
- [73] A. Gando et al. (KamLAND), Reactor On-Off Antineutrino Measurement with KamLAND, Phys. Rev. D 88, 033001 (2013), arXiv:1303.4667 [hep-ex].
- [74] A. Haghighat, P. Huber, S. Li, J. M. Link, C. Mariani, J. Park, and T. Subedi, Observation of Reactor Antineutrinos with a Rapidly-Deployable Surface-Level Detector, Phys. Rev. Applied 13, 034028 (2020), arXiv:1812.02163 [physics.ins-det].
- [75] A. Majumdar, D. K. Papoulias, R. Srivastava, and J. W. F. Valle, Physics implications of recent Dresden-II reactor data, Phys. Rev. D 106, 093010 (2022), arXiv:2208.13262 [hep-ph].
- [76] R. L. Workman et al. (Particle Data Group), Review of Particle Physics, PTEP 2022, 083C01 (2022).
- [77] J. Erler and M. J. Ramsey-Musolf, The Weak mixing angle at low energies, Phys. Rev. D 72, 073003 (2005), arXiv:hep-ph/0409169.
- [78] D. Akimov et al. (COHERENT), Measurement of the Coherent Elastic Neutrino-Nucleus Scattering Cross Section

- on CsI by COHERENT, Phys. Rev. Lett. ${\bf 129},~081801~(2022),~arXiv:2110.07730~[hep-ex].$
- [79] J. Guena, M. Lintz, and M. A. Bouchiat, Measurement of the parity violating 6S-7S transition amplitude in cesium achieved within $2 \times 10(-13)$ atomic-unit accuracy by stimulated-emission detection, Phys. Rev. A 71, 042108
- (2005), arXiv:physics/0412017.
- [80] M. Tanabashi *et al.* (Particle Data Group), Review of Particle Physics, Phys. Rev. D **98**, 030001 (2018).
- [81] J. Barranco, O. G. Miranda, and T. I. Rashba, Probing new physics with coherent neutrino scattering off nuclei, JHEP 12, 021, arXiv:hep-ph/0508299.